DOI: 10.1002/ejic.201001341

Control Over the Crystallinity and Defect Chemistry of YVO_4 Nanocrystals for Optimum Photocatalytic Property

Liusai Yang,[a] Guangshe Li,[b] Wanbiao Hu,[b] Minglei Zhao,[a] Lang Sun,[a] Jing Zheng,[a] Tingjiang Yan,[b] and Liping Li*[a]

Keywords: Vanadium / Yttrium / Nanoparticles / Crystal engineering / Photocatalysis

This work reports on the kinetic control over the crystallinity and defect chemistry of YVO_4 nanoparticles for the optimization of their photocatalytic performance. YVO_4 nanoparticles were prepared at room temperature via a precipitation method and then annealed in air at selected temperatures $\leq$ 500 °C to tune their crystallinity and defect features. By systematic evaluation of the sample characterizations, it has been found that the as-prepared samples crystallized in a pure tetragonal zircon-type structure, and the surfaces of the particles are hydrated. Upon annealing, all YVO_4 nanoparticles became dehydrated, which increased the crystallite sizes and improved the crystallinity of the samples. In contrast to many other oxide nanoparticles reported in literature, the increase in crystallite size of YVO_4 nanoparticles led to a lattice expansion, as observed by enhancement of the covalency of the V–O bonds and the systematic shifts in the Raman frequency modes, owing to the generation of oxygen vacancies on particle surfaces. The presence of oxygen vacancies not only introduced a deep acceptor level in the electronic structure that gives rise to a slightly narrowed bandgap and a broad visible emission, but also improved the photocatalytic activity of the particles; this latter effect is also a consesqence of the improved crystallinity of the samples.

Introduction

Semiconductor photocatalysts have received much attention due to their potential use in the degradation or complete mineralization of organic pollutants, which promises to solve current environmental problems with solar energy.[1] It is well established that photocatalytic activities of photocatalysts are strongly dependent on the intrinsic or extrinsic properties of catalysts such as particle size, morphology, crystallinity, and surface chemical states. Among these factors, the surface chemical states and crystallinity are commonly thought to play dominant roles in influencing the catalytic ability of the material. For instance, Amano et al.[2] studied the preparation of Bi_2WO_6 and found that the high crystallinity of this material greatly increased its photon absorption and photocatalytic efficiency. Similarly, Zhang et al.[3] observed the promoting role of crystallinity in the photocatalytic activity of nanosized TiO_2. In fact, all catalytic reactions occur on solid surfaces, and therefore the photocatalytic activities of semiconductors are also determined by the surface chemical states, e.g. cation defects, oxygen vacancies, and surface hydroxy groups. Great efforts have been devoted to modifying the surface structures of semiconductors via doping with various metal or nonmetal ions to enhance their optical absorption and photocatalytic performance.[4] During the doping processes, certain defects would be introduced into the semiconductor that may either positively or negatively impact its photocatalytic activity.[1c] Lattice defects do not enhance the photocatalytic activities of these compounds due to the high recombination rate of the photo-induced electrons and holes. Alternatively, oxygen vacancies on surfaces can be regarded as the desired defects for photocatalytic reactions because they can promote O_2 adsorption to capture photo-induced electrons to produce superoxide radicals, O_2^-, which in turn promote the oxidation of organic substances.[5] For almost all semiconductors, high crystallinity is often accompanied by low levels of defects. Consequently, the preparation of semiconductor photocatalysts with both good crystallinity and plentiful surface oxygen defects is challenging, but highly meaningful.

Tetragonal YVO_4 was taken as a model compound to study based on the following structural considerations: (1) In the YVO_4 lattice each isolated VO_4 tetrahedron is completely surrounded by YO_8 dodecahedra, and each YO_8 dodecahedron is connected to an adjacent YO_8 dodecahedron by a shared edge. For this type of crystal structure it is easy to introduce an imperfectly oxygen coordinated V site on

---

[a] Key Lab of Optoelectronic Materials Chemistry and Physics, Fujian Institute of Research on the Structure of Matter and Graduate School of Chinese Academy of Sciences,
Fuzhou 350002, P. R. China
Fax: +86-591-8370-2122
E-mail: lipingli@fjirsm.ac.cn
[b] State Key Lab of Structural Chemistry, Fujian Institute of Research on the Structure of Matter, Chinese Academy of Sciences,
Fuzhou 350002, P. R. China

Supporting information for this article is available on the WWW under http://dx.doi.org/10.1002/ejic.201001341.

the YVO_4 surface by heat treatment of the material; (2) previous investigations have shown that besides the oxygen defect color centers, oxygen vacancies can be introduced during annealing processes as demonstrated for as-grown YVO_4 crystals.[6] Point defects in semiconductors have been identified by electron paramagnetic resonance (EPR), a high resolution technique, although estimates of the defect concentrations for many compounds are limited by the fact that such measurements have been conducted at a very low temperature of ca. 10 K.[6b] It is well documented that defects in semiconductors may give rise to these materials having broad photoluminescence (PL) spectra in visible region.[7] Therefore, one can expect that the analysis of PL spectra will be helpful for studying the defects and the electronic structure that are relevant to the photochemical properties of YVO_4. Nobe et al. observed a broad emission band from 350 to 600 nm in the spectrum of undoped YVO_4 crystals and assigned it to the oxygen vacancies;[8] and (3) similar to other vanadium oxides such as $InVO_4$ and $FeVO_4$, YVO_4 has demonstrated promising photocatalytic activity.[9] Xu et al.[9c] found that the photocatalytic activity of YVO_4 nanocrystals gradually declined as their crystallinity increased, an effect which was simply attributed to the reduced specific surface area of the material.

It should be mentioned that the cooperative effect of crystallinity and surface oxygen vacancy concentration has an important role to play in achieving the excellent photocatalytic activity of YVO_4 nanoparticles. Careful control over these factors would be beneficial to understand the photocatalytic processes to be obtained, and to allow for the optimization of the photocatalytic properties of semiconductors. In this work, we prepared YVO_4 nanocrystals at room temperature by a direct precipitation method. The crystallinity and concentration of oxygen vacancies associated with the nanocrystals were controlled by subsequent annealing treatments at selected temperatures. The structures, Raman phonon frequencies, and photoluminescence emission properties of these YVO_4 nanoparticles were investigated to uncover the extent of the influence of the cooperative effect of crystallinity and oxygen vacancy concentration on the photocatalytic activity of YVO_4.

Results and Discussion

Formation of YVO_4 Nanoparticles and their Surface Hydration Chemistry

The phase composition of the as-synthesized YVO_4 nanoparticles (S-8.0) was examined by XRD. As indicated in Figure 1, all diffraction peaks well matched those of the standard diffraction data for YVO_4 (JCPDS, No. 82–1968), and no traces of extra diffraction peaks associated with other phases were observed. This indicates that S-8.0 crystallized in a single phase with a tetragonal zircon-type structure. All diffraction peaks were broad, which is characteristic of the constituent particles being small. The mean crystallite size that was estimated with the Scherrer formula based on peak (200) was ca. 5 nm, which is confirmed by TEM (inset, Figure 1). Further, all particles were seen to be aggregated severely, and had poor crystallinity and round morphology. The lattice fringes in the high resolution TEM image (Figure 1) were found to have a *d*-spacing of 0.3534 nm, which is in good agreement with the value of 0.3559 nm for the (200) planes in tetragonal YVO_4 (JCPDS, No. 82–1968). Therefore, the (100) surface predominates for all the nanoparticles.

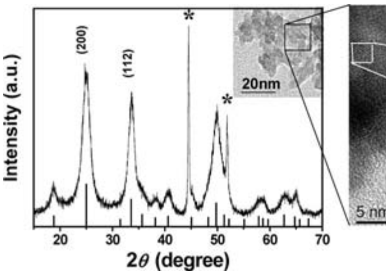

Figure 1. XRD pattern and TEM image (inset) of S-8.0. Asterisks * indicate peaks of the internal standard nickel. Vertical bars represent the standard diffraction data for bulk YVO_4 (JCPDS, No. 82–1968).

IR spectroscopy and thermogravimetric-mass spectrometry (TG-MS) were used to investigate the surface chemical states of S-8.0. As indicated in Figure 2, a broad absorption band was observed at ca. 3427 cm^{-1}, which is characteristic of the O–H stretching vibration of adsorbed water and O–H groups, while the absorption band at 1638 cm^{-1} is assigned to the bending mode of the associated water.[10] These observations confirm the presence of water molecules adsorbed on the surfaces of YVO_4 nanoparticles. As was observed for ZrO_2 prepared under aqueous basic conditions,[11] the surface hydration layers on YVO_4 nanoparticles have a relatively high activity towards the reaction with CO_2 (from air) to form carbonate species; the presence of such species on the surface of the YVO_4 particles was indicted by the appearance in the IR spectrum of two intense bands at 1509 and 1384 cm^{-1} that are associated with the symmetrical and asymmetrical vibrations of carboxylate groups. These carboxylate groups were desorbed from the particle surfaces when the material was annealed, as evidenced by the mass spectra of the exhaust gases produced during this process [Figure 3 (c)]. In the IR spectra for all YVO_4 nanocrystal samples investigated, a strong absorption band at 815 cm^{-1} and a weak band at 455 cm^{-1} were

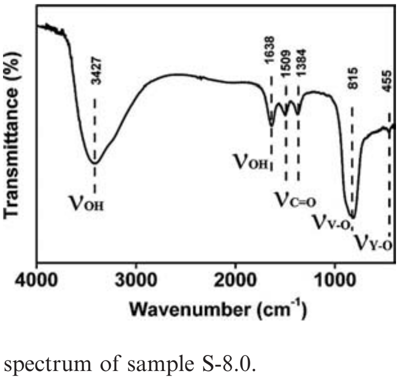

Figure 2. IR spectrum of sample S-8.0.

observed, which are characteristic of V–O and Y–O bond vibrations,[12] respectively. Therefore, the hydration layers are chemically bonded to the surfaces of the YVO_4 nanocrystals, which is similar to what has already been observed in other systems like TiO_2 and $CdWO_4$.[10a,13]

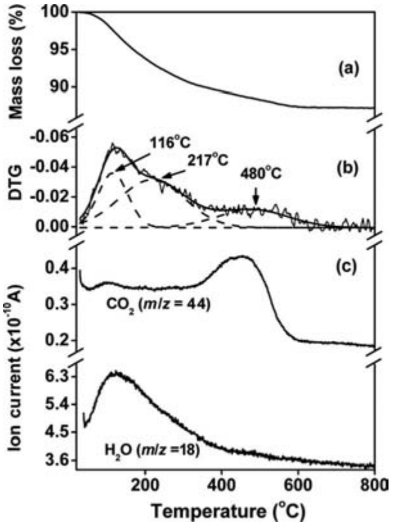

Figure 3. (a) TG curve, (b) DTG curve, and (c) mass spectra of S-8.0.

The surface hydration level for S-8.0 was quantitatively investigated by thermogravimetric (TG) analysis. As indicated in Figure 3 (a), S-8.0 exhibited a continuous mass loss from 30 to 600 °C, and a total mass loss of ca. 13 wt.-%. The differential thermal gravimetry (DTG) data showed that this mass loss process occurs in three steps, which have been modeled with Gaussian curves. As indicated in Figure 3 (b), the first Gaussian curve peaked at ca. 116 °C, and can be attributed to the desorption of the physisorbed water from the particle surfaces. The second peak appeared at 217 °C, and is due to the dehydration of chemisorbed water from the sample.[14] The last peak was centered at 480 °C, and is associated with the desorption of carbonate species from the particle surfaces. These assignments were confirmed by mass spectroscopy analysis of the exhaust gases released during the heating process [Figure 3 (c)]. Based on the area ratio of the three Gaussian components of the DTG curve, the mass losses related to the dehydration and desorption of carbonate species were determined to be 10.4 and 2.6 wt.-%, respectively.

Surface hydration is strongly associated with the surface chemical states and there is considerable interaction between the hydration layers and particle surfaces. As stated above, the water molecules bonded to the surfaces of YVO_4 nanocrystals can be divided into two groups: (i) physisorbed, and (ii) chemisorbed. As previously reported the chemisorbed water molecules are directly bonded to the nanoparticles through OH^- species,[10a] while the physisorbed water molecules are stabilized by hydrogen bonds with the adjacent bridging surface OH^- groups. Figure 4 illustrates the interactions between water molecules with the exposed (100) surface of YVO_4. For YVO_4 nanocrystals, the chemisorbed water molecules are likely to be anchored either to the surface cations (e.g. Y^{3+}, V^{5+}) or occupy the oxygen vacancy sites. Therefore, these water molecules are present in a wide range of energetically nonequivalent surface hydration groups, as indicated by the continuous mass loss from 30 to 600 °C in the TG data [Figure 3 (a)]. In spite of the strong interactions between the hydration groups and particle surfaces, the majority of the water molecules will be removed during the annealing process, and this will be followed by either the desorption of carbonate species from the surface, particle coarsening and/or more importantly, the alteration of the surface chemical states. A consequence of altering the surface chemical states can be the generation of surface and bulk defects, especially oxygen related defects, which can be expected to have a significant impact on the structural and physicochemical properties of YVO_4 nanocrystals.

The Impact of Annealing Hydrated YVO_4 Nanoparticles

Decreased Hydration Levels

As indicated by IR spectroscopic analysis (Figure S1), annealing samples of as-prepared YVO_4 nanoparticles between 300 and 500 °C did not change their hydration characteristics, while the total water content of the hydration layers was significantly changed. Increasing the annealing temperature decreased the total sample mass loss from 8 wt.-% for Z300, to 6 wt.-% for Z400, and to 2.7 wt.-% for Z500, where Z300, Z400, and Z500 are the names given to samples of S-8.0 annealed at 300, 400, and 500 °C, respectively (Figure S2). Further analysis of the mass loss observed for Z300 indicated that dehydration accounted for ca. 7 wt.-% of the loss compared to only 1.0 wt.-% loss resulting from the desorption of carbonate species. For both Z400 and Z500, the concentrations of carbonate species adsorbed on the nanoparticles are extremely low, and account for mass losses of less than 0.5 wt.-%, while majority of the total mass losses for these samples came from dehydration.

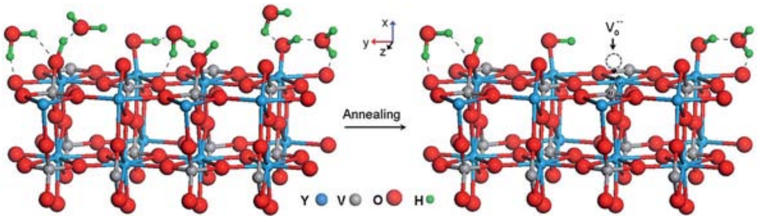

Figure 4. Scheme proposed for the behavior of water molecules decorating on the (100) surface of YVO_4 nanocrystals.

Nanoparticle Coarsening

Accompanied with the dehydration process are surface structural rearrangements as well as particle size or surface area changes. Specific surface areas of the annealed samples were investigated by evaluation of their nitrogen adsorption and desorption isotherm curves. S-8.0 has a surface area of $323\,m^2 g^{-1}$, which upon annealing is reduced to $229\,m^2 g^{-1}$ for Z300, then to $216\,m^2 g^{-1}$ for Z400, and finally to $95\,m^2 g^{-1}$ for Z500. As previously reported, the decrease in surface area is closely related to the coarsening of nanoparticles.[9c,9d]

Coarsening of YVO_4 nanoparticles did not destroy their single phase characteristics. As indicated in Figure 5 (a), no additional diffraction lines were observed for the particles after annealing, nevertheless all diffraction peaks gradually narrowed and sharpened, which corresponds to an increase in the crystallinity of the sample or particle growth from 6.8 nm for Z300, to 8.1 nm for Z400, and then to 9.8 nm for Z500. The coarsening of nanoparticles was also confirmed by TEM. From Figure 6, it can be seen that Z500 consists of relatively large aggregated particles with nearly spherical shape and an average particle size of ca. 10 nm, which is close to that calculated from the broadening of the diffraction peaks. The clear lattice fringes observed for a single particle demonstrated the enhanced crystallinity of the YVO_4 nanoparticles, and showed a plane space of 0.3574 nm, which is in accordance with that expected for the (200) plane. It is surprising that parts of these lattice fringes are discontinuous [inset of Figure 6 (b)], which can be associated with the generation of huge lattice defects[15] as a consequence of dehydration and the desorption of carbonate species during annealing, which was confirmed by photoluminescence emission studies (as addressed below). Similar phenomena were also observed for annealed TiO_2 nanoparticles.[5]

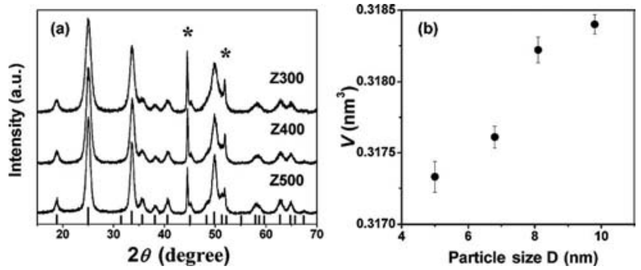

Figure 5. (a) XRD patterns of the annealed samples (Z300, Z400, Z500), and (b) particle size dependence of the unit cell volume (V) for YVO_4 nanoparticles. Asterisks * represent the diffraction lines associated with the internal standard nickel. The standard diffraction data for YVO_4 (JCPDS, No. 82–1968) are presented for comparison.

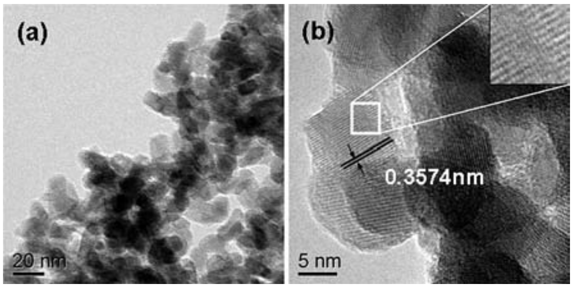

Figure 6. (a) TEM and (b) HRTEM images of Z500.

Lattice Expansion

Lattice parameters of the pre- and post-annealed samples were obtained by refining the XRD patterns by a least-squares method. The lattice parameters for S-8.0 were a = 7.109 (±0.001) Å and c = 6.279 (±0.001) Å, which expanded to a = 7.117 (±0.001) Å and c = 6.287 (±0.001) Å for Z500. Figure 5 (b) shows the relationship between the lattice volume and crystallite size for YVO_4 nanoparticles. With increasing crystallite size the lattice volume slightly increases. This result is interesting since it is different from what has been observed previously for many oxide nanoparticles,[13,16] for which grain growth leads to a decrease in the lattice volume owing to a decrease in the amount of surface defect dipoles.[17] In the present work, the lattice expansion observed for annealed nanoparticles could primarily be due to the increased concentration of oxygen vacancies, though a decrease in the amounts of defect dipoles may also contribute to the slightly reduced lattice volumes.

Oxygen vacancies in YVO_4 nanoparticles might be generated upon dehydration during the annealing process, since the OH^- species anchored to the surface cations (Figure 4) will be released, as described by the following Equation (1),

$$2\,OH_O^- \longrightarrow H_2O + O_O^x + V_O^{\bullet\bullet} \qquad (1)$$

where OH_O^-, O_O^x, $V_O^{\bullet\bullet}$ denote a hydroxy group in the oxygen ion site, oxygen ion on a lattice site, and an oxygen vacancy, respectively. In the YVO_4 lattice, some of the V^{5+} and Y^{3+} ions are threefold (3c) and sevenfold coordinated (7c), respectively. As a result, annealing may result in the formation of oxygen vacancies in the bulk, as well as the reduction of some of the bulk V^{5+} ions in accordance with the following Equation (2).

$$O_O^x \longrightarrow V_O^{\bullet\bullet} + O_2 \qquad (2)$$

Since an oxygen vacancy in the bulk lattice usually has dimensions smaller than that of an oxygen ion, it is highly probable that the occurrence of oxygen vacancies will give rise to a lattice constriction, different from what we observed for the annealed YVO_4 nanoparticles. This assumption is confirmed by theoretical simulations which show that the YVO_4 lattice volume increases when 0.125 mol of oxygen vacancies are introduced into the bulk lattice. However, the majority of oxygen vacancies could be located at the surfaces of the nanoparticles due to the "self-purified" effect.[18] As a result, oxygen vacancies on surfaces of YVO_4 nanoparticles would strengthen the outward repulsive force imposed on the surfaces causing a slight lattice expansion.

Changes in the Structural Vibrations

Closely related to the lattice expansion are the changes in the structural vibrations of the material upon annealing. In this reason, Raman spectra were collected to enable a comparative study of the structural vibrations of the pre- and post-annealed nanoparticles. As indicated in Figure 7, S-8.0 shows seven Raman vibration bands in the 100–1000 cm^{-1} range. It is well established that for the tetragonal zircon-type YVO_4 with D^{19}_{4h} symmetry (space group $I4_1/amd$), 26 optical modes are possible, which can be expressed by the following irreducible representation:[19] $\Gamma = 2A_{1g} + A_{2g} + 4B_{1g} + B_{2g} + 5E_g + A_{1u} + 4A_{2u} + B_{1u} + 2B_{2u} + 5E_u$. The vibration modes $2A_{1g} + 4B_{1g} + B_{2g} + 5E_g$ are Raman active, and modes $2A_{1g} + B_{2g} + 2B_{1g} + 2E_g$ are related to the internal vibrations of the tetrahedral VO_4^{3-} groups. Therefore, seven vibrational bands observed in the Raman spectra can be assigned accurately, as indicated in Figure 7. Among the observed bands, mode A_{1g}(I) has the highest intensity, while that associated with mode B_{1g}(II) shows the lowest intensity. It can also be seen in Figure 7 that S-8.0 exhibits broad and asymmetrical Raman peaks that become narrow and sharp after annealing, as indicated by the variations in the frequency half widths maxima of the peaks related to modes A_{1g}(I) and A_{1g}(II) (Figure S3). Moreover, the symmetry of the peaks increased for the samples after annealing, which indicates the improved crystallinity of the nanoparticles.[20]

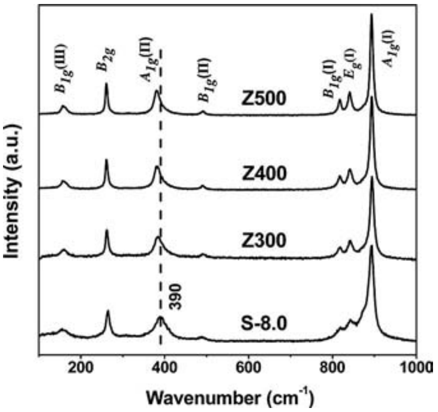

Figure 7. Raman spectra of the given YVO_4 nanoparticle samples.

In order to understand the influence of lattice expansion on the Raman modes, the Raman peak shifts for all samples were examined. Figure 8 shows the relationship between the Raman frequencies and YVO_4 nanoparticle cell volumes. It can be seen that modes E_g(I), and B_{2g} exhibited a systematic blue shift with increasing cell volume, which is in contrast to the red shift observed for mode A_{1g}(II), while modes A_{1g}(I), B_{1g}(I), B_{1g}(II), and B_{1g}(III) did not show noticeable shifts within the experimental errors with changing the cell volume. Linear fits to the data gave positive volume expansion coefficients of 3.4 ± 1.1 for mode E_g(I) and 2.6 ± 1.1 for B_{2g}, which are both smaller than the magnitude of the negative volume expansion coefficient of –6.5 ± 1.6 for A_{1g}(II). According to the lattice dynamics study of YVO_4,[21] almost all first-order Raman modes (except for B_{2g}) will shift towards higher frequencies with increasing the pressure, since under external pressure the YVO_4 lattice undergoes a constriction.[22] This means that most Raman modes for YVO_4 should have negative volume coefficients, which is not observed in this work. Indeed, Raman frequencies are theoretically dependent on the effective atomic masses and bond strengths. Compared to the external compressive pressure that only alters bond strengths, "chemical pressure" induced by introducing oxygen vacancies into the lattice could change both the effective atomic masses and bond strengths. Based on these considerations, it can be concluded that the positive volume expansion coefficient for the present YVO_4 nanocrystals is related to "chemical pressure" imposed by the oxygen vacancies, which have been identified by investigation of the luminescence properties for YVO_4 nanoparticles, as discussed below.

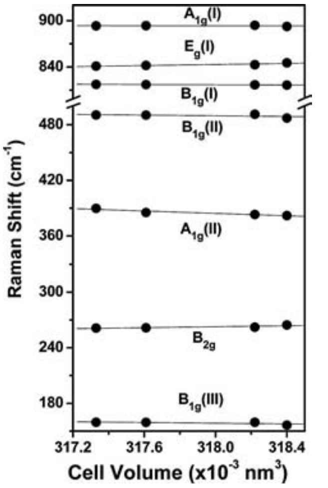

Figure 8. Cell volume dependency of the Raman peak frequencies for YVO_4 nanocrystals.

Impact of Annealing on the Luminescence Properties of YVO_4 Nanoparticles

For perfect YVO_4 crystals, no visible luminescent emission can be expected at room temperature because of the efficient diffusion of the thermal activation energy.[23] Nevertheless it has been frequently reported that when made into nanoparticles, YVO_4 displays visible emission that is related to the presence of defects. For instance, Qian et al. prepared self-assembled YVO_4 nano-persimmons and observed a broad emission in the 300–550 nm range of its spectrum when excited by 270 nm light.[24] Pankratov et al. also observed a blue emission for a YVO_4 single crystal that was assigned to a triplet exciton trapped near the defects of an oxygen vacancy.[25] The question is what are the luminescence properties of annealed YVO_4 nanocrystals?

Figure 9 exhibits the emission spectra of YVO_4 nanoparticles after 320 nm excitation. All samples displayed a broad blue emission in the 400–600 nm range in their spectra. Comparison of their emission spectra showed that the emission for S-8.0 is rather weak. Upon annealing of the material, its emission increased in intensity, while the peak center shifted from 470 nm for S-8.0 to 490 nm for Z500. This broad blue emission is not an intrinsic emission from the VO_4^{3-} groups, but originated from the defect centers in YVO_4 nanoparticles. Specifically, two kinds of defects may be expected: (1) oxygen vacancies or vanadium ions in low valence states such as V^{4+} or V^{3+}, and (2) a vanadium antisite defect caused by a V^{4+} ion substituting for a Y^{3+} ion.[6b]

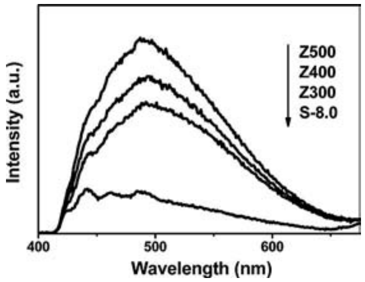

Figure 9. Photoluminescence spectra of given YVO_4 nanocrystals.

Numerous publications have indicated that oxygen vacancies or interstitial atoms in host lattices usually give rise to a broad band emission in their photoluminescence spectra. For instance, ZnO nanoparticles exhibit a strong broad emission that can be divided into several subpeaks situated at 415, 440, 455, and 488 nm, which arise from the transitions involving energy levels associated with the interstitial-zinc-related defect.[7c] For the present YVO_4 nanoparticles, owing to the annealing performed at relatively low temperatures, the dominant defects should be oxygen vacancies, followed by the formation of low valence vanadium ions. Therefore, defect complex centers like V^{4+}/V^{3+} will be adjacent to an oxygen vacancy. The increased emission intensity for the post-annealed samples confirms the increase in the concentration of oxygen vacancies, as reported by others.[8]

To determine if the defect complex centers account for the blue emission observed in the spectra reported in Figure 9, a theoretical simulation of YVO_4 with and without lattice oxygen vacancies was performed. For simplicity, only bulk vacancies were considered and the simulations were performed with a $2 \times 2 \times 1$ super-cell with $a = b = 12.509$ Å and $c = 6.214$ Å. As indicated in Figure 10 (a), the valence band for defect free YVO_4 is mainly composed of O2p orbitals, while the conduction band has contributions from the Y4s and V3d orbitals. The Fermi level, E_F, is at the top of valence band. It is noted that both the maximum of valence band (VB) and the minimum of the conduction band (CB) are at G (0,0,0), giving a band gap of c.a. 3.06 eV. This calculated band gap is slightly underestimated when compared to the previously reported data,[26] and this may be due to the well known limitation of the generalized gradient approximation (GGA) method.[27] Alternatively, when 3.125% of oxygen vacancies were included in the lattice, as illustrated in Figure 10 (b), the defective YVO_4 structure shows a deep acceptor level located in the band gap. This deep defect level is 2.33 eV above the top of the VB. Correspondingly, in the density of states (DOS) curve for the YVO_4 lattice with defects a small peak below the Fermi level can be seen. Owing to the introduction of the deep defect level, E_F shifted 2.72 eV from the top of VB. Accordingly, the energy difference between the minimum of the CB and the maximum of the VB is increased slightly to 3.11 eV. Based on these calculation results the visible emission for defective YVO_4 nanoparticles can be understood. During excitation by 320 nm light, electrons in YVO_4 would be excited from the VB to the CB, and upon jumping directly back into the VB will produce UV emission, alternatively the electron will drop down into the deep acceptor level before jumping back into the VB and producing a visible emission. It should be emphasized that the visible emission of YVO_4 originating from the radiative recombination of defect-bound excitons is very weak, which implies that most of the excited electrons did not take part in radiative recombination. Therefore, it may be expected that YVO_4 with oxygen vacancy defects will exhibit photocatalytic activity under UV light irradiation.

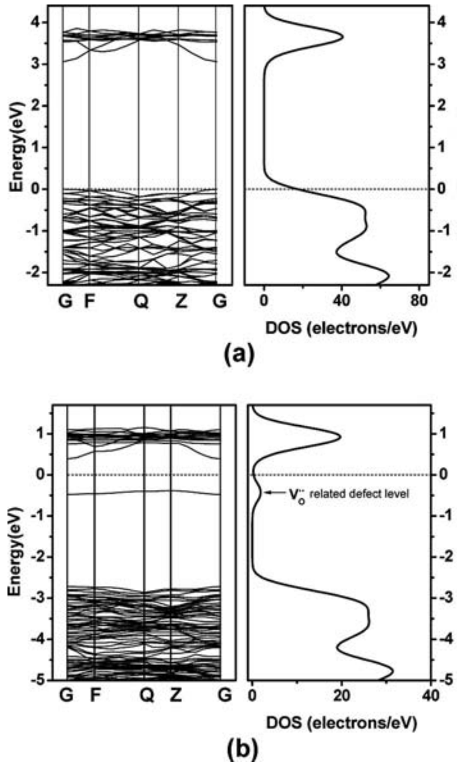

Figure 10. Electronic structures and density of states (DOS) of (a) defect free YVO_4 and (b) YVO_4 with lattice oxygen vacancies.

UV/Vis diffuse reflectance spectroscopy has been used to study the electronic transition in YVO_4. As indicated in Figure 11, all samples exhibited broad asymmetrical absorption bands in the 200–370 nm range of their spectra, which can be ascribed to the charge transfer from oxygen ligands to the central vanadium atoms inside the VO_4^{3-} complexes.[28] The data were fit with two Gaussian functions, which allowed for the low energy subabsorption to be assigned to ${}^1A_1 \rightarrow {}^1T_1$ transitions in VO_4^{3-}, and the high energy subabsorption to be associated with ${}^1A_1 \rightarrow {}^1T_2$ transitions.[29] Table 1 summarizes the data fitting results for all samples, including details of the peak positions and intensity ratios (I_2/I_1) for transitions $^1A_1 \rightarrow {}^1T_2$ (with intensity I_2) and $^1A_1 \rightarrow {}^1T_1$ (with intensity I_1). It can be seen that once the material has been annealed at 400 and 500 °C, the intensity ratio I_2/I_1 decreases relative to S-8.0. According to the molecular orbital theory, $^1A_1 \rightarrow {}^1T_2$ is a symmetry allowed transition, while $^1A_1 \rightarrow {}^1T_1$ is symmetry forbidden.[29] The decrease in the intensity ratio I_2/I_1 implies that the defects produced during annealing could partially allow the symmetry forbidden transitions to occur. It is also noted that after annealing, the bands associated with the $^1A_1 \rightarrow {}^1T_1$ and $^1A_1 \rightarrow {}^1T_2$ transitions shifted to longer wavelengths (i.e. lower energy), which demonstrates the increased covalence of the V–O bonds, as has also been observed in other systems.[30]

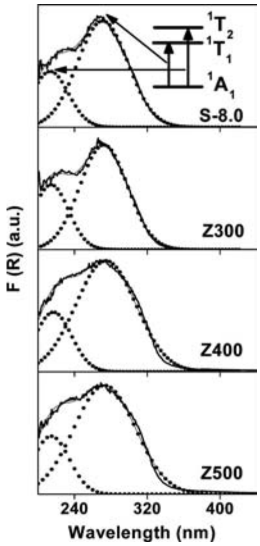

Figure 11. Diffuse reflectance spectra of given YVO_4 nanocrystals. All spectroscopic data were fitted with Gaussian functions. Inset is a sketch of the electronic transitions corresponding to both Gaussian components.

Table 1. Data fit results for the diffuse reflectance spectra of YVO_4 nanoparticles.

Sample	Peak position [nm]		I_2/I_1	Band gap [eV]
	$^1A_1 \rightarrow {}^1T_2$	$^1A_1 \rightarrow {}^1T_1$		
S-8.0	213.3 ± 0.3	271.0 ± 0.1	0.38	3.97 ± 0.09
Z300	214.3 ± 0.4	272.1 ± 0.2	0.45	3.96 ± 0.09
Z400	216.7 ± 0.4	274.5 ± 0.3	0.32	3.78 ± 0.09
Z500	214.4 ± 0.3	273.1 ± 0.3	0.31	3.77 ± 0.09

Band gap energies for all YVO_4 nanoparticles were calculated on the basis of their diffuse reflectance spectra. For an idealized parabolic band *bulk* semiconductor with allowed transitions, the optical absorption edge can be fit with the Tauc equation 3,[31]

$$ah\nu = K(h\nu - E_g)^{1/n} \qquad (3)$$

where a is the absorption coefficient, K is the characteristic constant of semiconductors, $h\nu$ and E_g are the photon energy and optical band gap energy, respectively, and n equals 2 since YVO_4 is a direct semiconductor as indicated by the above mentioned theoretical simulations and previous reports.[32] Therefore, the E_g values can be determined by extrapolation of the linear portion of the $(ah\nu)^2$ vs. photon energy curve, i.e. from $h\nu$ to $(ah\nu)^2 = 0$ (Figure S4). As listed in Table 1, the bang gap energy for S-8.0 is 3.97 eV, which remained almost constant when the sample was annealed at 300 °C. Annealing the nanoparticles up to a temperature of 500 °C led to E_g decreasing to 3.77 eV. Even so, the band gap energies for the present nanoparticles were all larger than the value of 3.28 eV for bulk YVO_4.[26] These observations can be understood by taking into account the annealing-induced grain growth and the improved surface band bending due to the dehydration and desorption of carbonate species, as described by the above in the discussion of the TG analysis; these findings are commonly observed during the growth of semiconductor nanocrystals.[33]

Impact of Annealing on the Photocatalytic Activity of YVO_4 Nanoparticles

The photocatalytic activities of YVO_4 nanoparticles were evaluated by investigating their ability to degrade an aqueous solution rhodamine B (RhB) under UV light irradiation. To confirm the photocatalytic ability of the YVO_4 nanoparticles, two parallel experiments were performed to exclude the possible influences of the self-degradation of RhB under UV light irradiation and the adsorption of RhB molecules onto the surfaces of the YVO_4 nanoparticles. As shown in Figure S5a, the absorption spectra of RhB solutions without YVO_4 nanoparticles exhibited a gradual decrease in the intensity of the RhB signals with UV irradiation, which suggests that the RhB solution probably exhibits some self-degradation. Dark reaction data (Figure S5b) indicated that after stirring for 40 min, the RhB molecules reached an adsorption balance with the YVO_4 nanoparticles. With these results in mind, the photocatalytic activities of YVO_4 nanoparticles, with and without annealing, were investigated under UV light irradiation. Figure 12 compares the absorption spectra of RhB solutions when S-8.0 and Z500 were added to them. In the presence of S-8.0 the absorption peak for RhB seen at 554 nm in the spectra decreased slowly with prolonging the irradiation time. Even when the irradiation time was prolonged to 80 min, this RhB absorption peak was still observable in the spectra of the reaction solution. Conversely, the RhB absorption peak disappeared in the presence of Z500 after only 40 min of irradiation. Figure 13 (a) shows the normalized absorbance changes of all solutions under UV light as a function of irradiation time. The relative intensity ratio, C/C_0, for the spectra recorded for the reaction solution containing S-8.0 was 0.35 after 80 min irradiation, which is much smaller than the value of 0.57 recorded for the blank experiment (Figure S5c). Therefore, the degradation of RhB molecules is improved by introducing S-8.0 into the reaction solution. When an annealed YVO_4 sample is added to the reaction solution, the C/C_0 ratio decreases further after the same amount irradiation time, which indicates the improved photocatalytic activity of the annealed YVO_4 relative to S-8.0. The times required for complete degradation of the RhB molecules in the presence of Z300, Z400, and Z500 were about 70, 55, and 45 min, respectively.

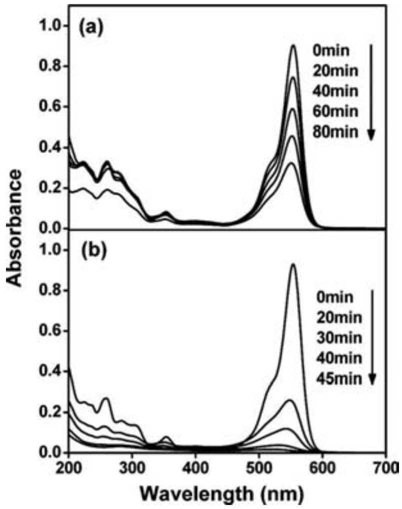

Figure 12. Time dependent absorption spectra of RhB solutions in the presence of (a) S-8.0 and (b) Z500 under UV light irradiation.

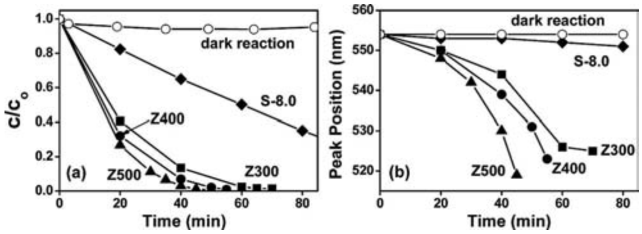

Figure 13. (a) Variations in the relative intensity C/C_0, and (b) shifts of the RhB absorption peak position in spectra of RhB solutions containing YVO_4 nanoparticles, as functions of irradiation time.

As indicated in Figure 13 (b), in addition to the intensity variations, the RhB solution absorption peaks also shifted to lower wavelengths relative to the peaks in the spectra of the nonirradiated solutions. After 40 min of irradiation, a large shift of 20 nm was observed for the solution containing Z500, which is possibly due to the formation of photodegradation intermediate species. Chen et al.[34] separated the intermediates from RhB photodegradation, and found that these intermediates are *N*,*N*-diethyl-*N′*-ethylrhodamine, *N*-ethyl-*N′*-ethylrhodamine, *N*,*N*-diethylrhodamine, *N*-ethylrhodamine, which show absorption maxima at 537, 527, 522, and 512 nm, respectively. The absorption maximum observed at ca. 519 nm in the spectra of the RhB solutions containing Z500 implies that *N*-ethylrhodamine has been formed. It is thus concluded that RhB molecules in aqueous solutions were effectively degraded in the presence of YVO_4 nanoparticles under UV light irradiation, and that annealing of the nanoparticles may promote their photocatalytic activity.

To explain the enhanced photocatalytic activity of the annealed nanoparticles relative to S-8.0, the crystallinity and defect concentration of the samples are the two primary factors that should be addressed. The crystallinity of a material is known to have a great influence on its photocatalytic activity. A nanoparticles' crystallinity is usually related to the status of its surface where a layer of amorphous-like disorder may occur due to the adsorption of water and carbonate species, and this implies poor particle crystallinity. These adsorbed species would hinder the interaction between the nanoparticle surface and dye molecules, which will certainly reduce the reaction activity of the particle. As a consequence, when the adsorbed species are removed during the annealing process, the activity of the particle will increase, due to its increased crystallinity. Similarly, Amino et al.[2] studied Bi_2WO_6 and found that increasing this compound's crystallinity improves its photocatalytic activity because of its increased ability to absorb photons. Zhang et al.[3] ascribed the enhanced photoactivity of nanosized TiO_2 to improvements in the material's crystallinity at the nanoscale. Our recent work with $CdWO_4$ nanoparticles confirmed the dependence of photocatalytic activity on the particle crystallinity.[13] Compared to S-8.0, all three annealed samples showed improved photocatalytic activity, which is consistent with their enhanced crystallinity.

As stated above, annealing the YVO_4 nanoparticles also led to the generation of oxygen vacancies, which may accelerate the photo-degradation of RhB. This is because the increased concentration of oxygen vacancies can promote O_2 adsorption at surfaces, and serve as the centers to capture the photo-induced electrons during the photocatalytic reaction processes thus inhibiting recombination of the photo-induced charge carriers, which in turn will increase the photocatalytic activities of the annealed nanoparticles.[35] Sample Z500 has the combined features of both high crystallinity and high oxygen vacancy concentration, which accounts for why it has best photocatalytic activity of all the samples reported herein.

Conclusions

YVO_4 nanoparticles with different degrees of crystallinity and oxygen vacancy concentrations were synthesized at room temperature by a precipitation method, and were annealed at low temperatures (≤500 °C). All as-prepared YVO_4 nanoparticles featured surface hydration, which upon annealing was removed to give a slightly increased crystallite size, enhanced crystallinity, and the production of abundant oxygen vacancies on the particle surfaces. All of these factors influence the surface chemistry of nanoparticles, and are important for tailoring their structural and physicochemical properties. Furthermore, lattice expansion was observed in YVO_4 nanoparticles upon annealing, which was explained in terms of a strengthened repulsive force on the particle surfaces due to the presence of oxygen vacancies. By obtaining a balance between the concentration of oxygen vacancies and particle crystallinity, the photocatalytic activity of YVO_4 nanoparticles was optimized. The results reported here are highly promising for improving our ability to manipulate nanocrystal defect chemistry to increase the particle functionality.

Experimental Section

Sample Preparation: YVO_4 nanoparticles were prepared at room temperature by a precipitation method. Analytical grade chemicals, $Y(NO_3)_3{\cdot}6H_2O$, NH_4VO_3, and NaOH were used as the starting materials. All reagents were purchased from Shanghai Chemical Reagent Company and were used as received without further purification. The synthetic procedure for all the samples is as follows: $Y(NO_3)_3{\cdot}6H_2O$ (2.300 g, 6.0 mmol) was dissolved in distilled water (105 mL) with stirring to form transparent **solution I**. NH_4VO_3 (0.7019 g, 6.0 mmol) and NaOH (20 mL, 0.5 mol L^{-1}) were dissolved in distilled water (60 mL) to form **solution II**. Then, **solution II** was rapidly added to **solution I** to obtain a white suspension. After adjusting the pH of the suspension to ca. 8.0 with NaOH solution (0.5 mol L^{-1}), the mixture was stirred for 3 h at room temperature. Finally, the white precipitate was separated from the solution by centrifugation, washed with distilled water, and then dried at 80 °C in air. The as-prepared sample was named S-8.0.

To gain an insight into the crystallinity and oxygen vacancy concentration of the YVO_4 nanocrystals, the as-prepared sample S-8.0 was annealed in air at lower temperatures of 300, 400, and 500 °C for 2 h, and the corresponding products were denoted as Z300, Z400, and Z500, respectively.

Sample Characterization: Sample structures were characterized by XRD. XRD data were collected on a Rigaku MiniFlex II benchtop X-ray diffractometer with a copper target. D, the average crystallite size, was calculated from the (200) diffraction peak by the Scherrer formula $D = 0.9\lambda/(\beta\cos\theta)$, where λ is the X-ray wavelength employed, θ is the diffraction angle of the (200) diffraction peak, and β is defined as the half –width of the peak after correction for instrumental broadening effects. Lattice parameters for the samples were calculated by a least-squares method with Rietica Rietveld software. Ni powder served as an XRD internal standard to allow for peak position determination. Infrared spectra of the samples were measured on a Perkin–Elmer IR spectrophotometer with a a resolution of 4 cm^{-1} by the KBr pellet technique.

The particle size and morphology of the samples were observed by transmission electron microscopy (TEM) performed on a JEM-2010 apparatus with an acceleration voltage of 200 kV. UV/Vis diffuse reflectance spectra of the samples were recorded over the 200–800 nm range on a Varian Cary 500 scan UV/Vis/NIR spectrophotometer with $BaSO_4$ as the background. Emission spectra were measured on an Edinburgh Instruments FLS920 spectrofluorimeter equipped with both continuous (450 W) and pulsed xenon lamps. The thermal behaviors of samples were examined by TA measurements carried out on a STA 449C at a heating rate of 15 K/min over the 30–800 °C range, in an flowing N_2 atmosphere with a flux of 30 mL min^{-1}. The specific surface areas of the samples were determined from nitrogen absorption data recorded at 150 °C by the Barrett–Emmett–Teller (BET) technique performed on a Micromerities ASAP 2000 surface area and porosity analyzer. Raman spectra of the samples were obtained on a Renishaw Raman microscope InVia Plus system with an excitation line of 785 nm.

Theoretical Calculation of Electronic Structures: The electronic structures of YVO_4 in different states were calculated on the basis of plane-wave density function theory with the Castep package in the Material Studio software.[36] Vanderbilt-type ultrasoft pseudopotentials (USPP) were employed to describe the electron-ion interactions. The generalized gradient approximation (GGA) in the scheme of Perdew–Burke–Eruzerhof (PBE) was used to describe the exchange and correlation terms. After geometry optimization, and consideration of the 3d electrons of the V ions, the GGA+U approach was employed to investigate the electronic structures of the materials. The value U of Hubbard was fixed at 2.5 eV.[37]

Photocatalytic Activity Test: The photocatalytic activity measurements of the samples were carried out on solutions in a quartz tube with an inner diameter of 4.6 cm and 17 cm in length. The reaction solution was surrounded by four 4-Watt UV lamps set with a wavelength centered at 254 nm (Philips, TUV 4 Watt/G4 T5). The YVO_4 sample (100 mg) was suspended in an aqueous solution of rhodamine B (RhB) (150 mL, 1×0^{-5} м) . Prior to irradiation the suspension was magnetically stirred in the dark for 1 h to establish an adsorption-desorption equilibrium. During the experiments, 3 mL aliquots of the reaction solutions were collected every 10 min and centrifuged to remove the samples. The filtrates were analyzed on a Perkin–Elmer UV WinLab Lambda 35 spectrophotometer. The degradation percentage is reported as C/C_0, where C is the intensity of the peak at 554 nm, which is assigned to RhB, in the spectra of the collected aliquots, and C_0 is the absorption intensity of the same peak in the spectrum of the initial rhodamine B solutions once the adsorption–desorption equilibrium was achieved.

Supporting Information (see footnote on the first page of this article): IR spectra, TG curves, particle size dependence of the full width at half maximum of the Raman vibrations, and the energy dependence of $(\alpha h\nu)^2$ for annealed YVO_4 nanoparticles, time dependent absorption spectra for a RhB solution without YVO_4 nanoparticles recorded under UV light irradiation.

Acknowledgments

This work was financially supported by the Natural Science Foundation of China (NSFC, grant numbers 50972143, 51072198 and 20831004), the National Basic Research Program of China (grant numbers 2009CB939801, 2007CB613301), and fund of 2006L2005.

---

[1] a) S. Sakthivel, B. Neppolian, M. V. Shankar, B. Arabindoo, M. Palanichamy, V. Murugesan, *Sol. J. Energ. Mater Sol. Cells* **2003**, *77*, 65–82; b) D. Chatterjee, S. Dasgupta, *J. Photochem. Photobiol. C: Photochem. Rev.* **2005**, *6*, 186–205; c) T. L. Thompson, J. T. Yates, *Chem. Rev.* **2006**, *106*, 4428–4453.
[2] F. Amano, A. Yamakata, K. Nogami, M. Osawa, B. Ohtani, *J. Am. Chem. Soc.* **2008**, *130*, 17650–17651.
[3] Q. H. Zhang, L. Gao, J. K. Guo, *Appl. Catal. B: Environ.* **2000**, *26*, 207–215.
[4] a) R. Asahi, T. Morikawa, T. Ohwaki, K. Aoki, Y. Taga, *Science* **2001**, *293*, 269–271; b) S. Mozia, M. Tomaszewska, B. Kosowska, B. Grzmil, A. W. Morawski, K. Kalucki, *Appl. Catal. B: Environ.* **2005**, *55*, 195–200; c) J. C. Yu, J. G. Yu, W. K. Ho, Z. T. Jiang, L. Z. Zhang, *Chem. Mater.* **2002**, *14*, 3808–3816.
[5] T. L. Thompson, J. T. Yates, *Top. Catal.* **2005**, *35*, 197–210.
[6] a) N. Y. Garces, L. E. Halliburton, K. T. Stevens, M. Shone, G. K. Foundos, *J. Appl. Phys.* **2002**, *91*, 1354–1358; b) N. Y. Garces, K. T. Stevens, G. K. Foundos, L. E. Halliburton, *J. Phys.: Condens. Matter* **2004**, *16*, 7095–7106.
[7] a) L. P. Li, Y. G. Su, G. S. Li, *J. Mater. Chem.* **2010**, *20*, 459–465; b) H. B. Zeng, W. P. Cai, P. S. Liu, X. X. Xu, H. J. Zhou, C. Klingshirn, H. Kalt, *ACS Nano* **2008**, *2*, 1661–1670; c) H. B. Zeng, G. T. Duan, Y. Li, S. K. Yang, X. X. Xu, W. P. Cai, *Adv. Funct. Mater.* **2010**, *20*, 561–572.

[8] Y. Nobe, H. Takashima, T. Katsumata, *Opt. Lett.* **1994**, *19*, 1216–1218.

[9] a) L. W. Zhang, H. B. Fu, C. Zhang, Y. F. Zhu, *J. Solid State Chem.* **2006**, *179*, 804–811; b) J. H. Deng, J. Y. Jiang, Y. Y. Zhang, X. P. Lin, C. M. Du, Y. Xiong, *Appl. Catal. B: Environ.* **2008**, *84*, 468–473; c) H. Y. Xu, H. Wang, H. Yan, *J. Hazard. Mater.* **2007**, *144*, 82–85; d) Y. Liu, J. F. Ma, C. H. Dai, Z. W. Song, Y. Sun, J. R. Fang, C. Gao, J. G. Zhao, *J. Am. Ceram. Soc.* **2009**, *92*, 2791–2794.

[10] a) G. S. Li, L. P. Li, J. Boerio-Goates, B. F. Woodfield, *J. Am. Chem. Soc.* **2005**, *127*, 8659–8666; b) W. B. Hu, L. P. Li, G. S. Li, J. Meng, W. M. Tong, *J. Phys. Chem. C* **2009**, *113*, 16996–17001.

[11] H. Wang, G. S. Li, Y. F. Xue, L. P. Li, *J. Solid State Chem.* **2007**, *180*, 2790–2797.

[12] M. Yu, J. Lin, Z. Wang, J. Fu, S. Wang, H. J. Zhang, Y. C. Han, *Chem. Mater.* **2002**, *14*, 2224–2231.

[13] W. M. Tong, L. P. Li, W. B. Hu, T. J. Yan, G. S. Li, *J. Phys. Chem. C* **2010**, *114*, 1512–1519.

[14] J. F. Boily, J. Szanyi, A. R. Felmy, *Geochim. Cosmochim. Acta* **2006**, *70*, 3613–3624.

[15] a) F. Wang, X. J. Xue, X. G. Liu, *Angew. Chem. Int. Ed.* **2008**, *47*, 906–909; b) X. W. Liu, K. B. Zhou, L. Wang, B. Y. Wang, Y. D. Li, *J. Am. Chem. Soc.* **2009**, *131*, 3140–3141.

[16] a) F. Zhang, S. W. Chan, J. E. Spanier, E. Apak, Q. Jin, R. D. Robinson, I. P. Herman, *Appl. Phys. Lett.* **2002**, *80*, 127–129; b) L. P. Li, Y. G. Su, G. S. Li, *Appl. Phys. Lett.* **2007**, *90*, 054105; c) W. B. Hu, L. P. Li, W. M. Tong, G. S. Li, T. J. Yan, *J. Mater. Chem.* **2010**, *20*, 8659–8667.

[17] a) G. S. Li, J. Boerio-Goates, B. F. Woodfield, L. P. Li, *Appl. Phys. Lett.* **2004**, *85*, 2059–2061; b) V. Swamy, D. Menzies, B. C. Muddle, A. Kuznetsov, L. S. Dubrovinsky, Q. Dai, V. Dmitriev, *Appl. Phys. Lett.* **2006**, *88*, 243103.

[18] a) G. Hodes, *Adv. Mater.* **2007**, *19*, 639–655; b) X. B. Chen, G. S. Li, Y. G. Su, X. Q. Qiu, L. P. Li, Z. G. Zou, *Nanotechnology* **2009**, *20*, 115606.

[19] Y. K. Voron'ko, A. A. Sobol, V. E. Shukshin, A. I. Zagumennyi, Y. D. Zavartsev, S. A. Kutovoi, *Phys. Solid State* **2009**, *51*, 1886–1893.

[20] K. N. Yu, X. H. Xiong, Y. L. Liu, C. S. Xiong, *Phys. Rev. B* **1997**, *55*, 2666–2671.

[21] F. J. Manjon, P. Rodriguez-Hernandez, A. Munoz, A. H. Romero, D. Errandonea, K. Syassen, *Phys. Rev. B* **2010**, *81*, 075202.

[22] X. Wang, I. Loa, K. Syassen, M. Hanfland, B. Ferrand, *Phys. Rev. B* **2004**, *70*, 064109.

[23] G. Blasse, *Luminescent Materials*, Springer, Berlin, Germany, **1999**.

[24] L. W. Qian, J. Zhu, Z. Chen, Y. C. Gui, Q. Gong, Y. P. Yuan, J. T. Zai, X. F. Qian, *Chem. Eur. J.* **2009**, *15*, 1233–1240.

[25] V. Pankratov, L. Grigorjeva, D. Millers, H. M. Yochum, in: *Physica Status Solidi C - Current Topics in Solid State Physics*, (Ed.: M. Stutzmann), Wiley-VCH, Weinheim, Germany, **2007**, vol. 4, pp. 801–804.

[26] O. Mistautake, B. Mauro, M. Akiyuki, Y. JinHua, *Mater. Res. Soc.* **2009**, *1171*, 03.

[27] Z. Rak, S. D. Mahanti, K. C. Mandal, N. C. Fernelius, *J. Phys.: Condens. Matter* **2009**, *21*, 015504.

[28] G. A. Jia, Y. H. Song, M. Yang, Y. J. Huang, L. H. Zhang, H. P. You, *Opt. Mater.* **2009**, *31*, 1032–1037.

[29] H. Ronde, G. Blasse, *J. Inorg. Nucl. Chem.* **1978**, *40*, 215–219.

[30] L. R. Singh, R. S. Ningthoujam, *J. Appl. Phys.* **2010**, *107*, 104304.

[31] V. M. Huxter, T. Mirkovic, P. S. Nair, G. D. Scholes, *Adv. Mater.* **2008**, *20*, 2439–2443.

[32] Z. P. Ci, Y. H. Wang, J. C. Zhang, *Chin. Phys. B* **2010**, *19*, 057803.

[33] a) A. D. Yoffe, *Adv. Phys.* **2001**, *50*, 1–208; b) K. F. Lin, H. M. Cheng, H. C. Hsu, L. J. Lin, W. F. Hsieh, *Chem. Phys. Lett.* **2005**, *409*, 208–211.

[34] C. C. Chen, W. Zhao, P. X. Lei, J. C. Zhao, N. Serponer, *Chem. Eur. J.* **2004**, *10*, 1956–1965.

[35] a) C. Belver, R. Bellod, S. J. Stewart, F. G. Requejo, M. Fernandez-Garcia, *Appl. Catal. B: Environ.* **2006**, *65*, 309–314; b) Y. H. Zheng, C. Q. Chen, Y. Y. Zhan, X. Y. Lin, Q. Zheng, K. M. Wei, J. F. Zhu, Y. J. Zhu, *Inorg. Chem.* **2007**, *46*, 6675–6682.

[36] V. Milman, B. Winkler, J. A. White, C. J. Pickard, M. C. Payne, E. V. Akhmatskaya, R. H. Nobes, *Int. J. Quantum Chem.* **2000**, *77*, 895–910.

[37] H. Sawada, K. Terakura, *Phys. Rev. B* **1998**, *58*, 6831–6836.

Received: December 22, 2010